Unveiling the Phase Diagram and Reaction Paths of the Active Model B with the Deep Minimum Action Method

Ruben Zakine, Eric Simonnet, Eric Vanden-Eijnden

Unveiling the Phase Diagram and Reaction Paths of the Active Model B with the Deep Minimum Action Method

Ruben Zakine,[1,2,3] Eric Simonnet,[4] and Eric Vanden-Eijnden[1]

[1]*Courant Institute, New York University, 251 Mercer Street, New York, New York 10012, USA*
[2]*Chair of Econophysics and Complex Systems, École Polytechnique, 91128 Palaiseau Cedex, France*
[3]*LadHyX UMR CNRS 7646, École Polytechnique, 91128 Palaiseau Cedex, France*
[4]*INPHYNI, Université Côte d'Azur et CNRS, 17 rue Julien Lauprêtre 06200 Nice, France*

(Dated: November 21, 2024)

Nonequilibrium phase transitions are notably difficult to analyze because their mechanisms depend on the system's dynamics in a complex way due to the lack of time-reversal symmetry. To complicate matters, the system's steady-state distribution is unknown in general. Here, the phase diagram of the active Model B is computed with a deep neural network implementation of the geometric minimum action method (gMAM). This approach unveils the unconventional reaction paths and nucleation mechanism in dimensions 1, 2 and 3, by which the system switches between the homogeneous and inhomogeneous phases in the binodal region. Our main findings are: (i) the mean time to escape the phase-separated state is (exponentially) extensive in the system size L, but it increases *non-monotonically* with L in dimension 1; (ii) the mean time to escape the homogeneous state is always finite, in line with the recent work of Cates and Nardini [1]; (iii) at fixed L, the active term increases the stability of the homogeneous phase, eventually destroying the phase separation in the binodal for large but finite systems. Our results are particularly relevant for active matter systems in which the number of constituents hardly goes beyond 10^7 and where finite-size effects matter.

Introduction– Activated processes, pervasive in nature, are intrinsically difficult to probe in simulations since they require the sampling of rare events [2–5]. When a first-order phase transition (FOPT) occurs, a nucleation event is usually required for the system to reach its stable phase [1, 6–8]. In equilibrium systems, we can exploit the property of time-reversal symmetry (TRS) and the knowledge of their equilibrium distribution to derive a free energy from which we can infer both the thermodynamic stability of each phase, and the reaction paths that are followed by the system during activation [9–11]. However, TRS breakdown in nonequilibrium systems prevents access to the free energy, necessitating comprehension of activated process mechanisms through dynamics rather than unknown steady-state distributions [12–19]. Mapping their phase diagram thus persists as a challenge.

In this letter, we tackle this issue within the active Model B, a natural nonequilibrium extension of Cahn-Hilliard dynamics with a nonlinear growth term [20, 21] breaking TRS. This widely studied model has attracted considerable attention in recent years [22–25], serving as an effective description, for instance, of active particles undergoing motility-induced phase separation (MIPS) [26–28]. Here, we map the phase diagram of the active Model B and analyze FOPT pathways. Our findings reveal transitions involving nucleation events markedly different from their equilibrium counterparts, shaped by the interplay between noise and nongradient terms in the stochastic system dynamics. Moreover, in large but finite systems, we demonstrate that the active term can reduce the probability of observing phase-separated state nucleation and facilitate the reverse transition from the phase-separated phase to the homogeneous state. To obtain these results, we compute reaction paths using a geometric Minimum Action Method (gMAM) [29–31] implementation relying on Physics-Informed Neural Networks (PINNs) [32, 33]. This neural implementation, known as deep gMAM [34], is notable as it can be transferred to study FOPTs in other nonequilibrium systems. It also gives access to higher dimensional problems not accessible by traditional methods. Additionally, we cross-check some results of the deep gMAM algorithm using the traditional gMAM method as a benchmark.

Problem setting– The active Model B (AMB) characterizes the stochastic dynamics of a conserved scalar field $\phi(x,t)$, usually interpreted as the local (relative) density of particles or the local composition of a mixture. It can be expressed as the divergence of a noisy flux [1, 22, 23, 35]

$$\partial_t \phi = \nabla \cdot (M \nabla \mu + \xi), \tag{1}$$

$$\mu([\phi], x) = \frac{\delta \mathcal{F}[\phi]}{\delta \phi(x)} + \lambda |\nabla \phi(x)|^2, \tag{2}$$

In this context, $\mathcal{F}[\phi]$ represents a Ginzburg-Landau free energy, M is the mobility operator, and ξ is a spatio-temporal white noise, a Gaussian process with mean zero and covariance $\langle \xi(x,t)\xi(x',t')\rangle = 2\epsilon M \delta(x-x')\delta(t-t')$, where ϵ controls the amplitude of fluctuations. We investigate Eq. (1) in $d = 1$ up to $d = 3$ dimensions, assuming periodic boundary conditions of the domain $\Omega = [0, L]^d$ with lateral size L. We simplify by considering $M = \mathbb{1}$ and $\mathcal{F}[\phi] = \int_\Omega [\frac{1}{2}\nu(\nabla\phi)^2 + f(\phi)]dx$, where $\nu > 0$ and $f(\phi)$ represents a double-well potential. With this choice, there is a region of the phase diagram where a homogeneous state, denoted ϕ_H, coexists with a phase-separated state (or inhomogeneous state), denoted ϕ_I (see Fig. 1(a)). These states correspond to the two locally stable fixed points of the noiseless version of Eq. (1), namely the solution to $\nabla \cdot (M\nabla\mu) = 0$ with a prescribed value of the spatial average ϕ_0 of ϕ in the domain.

When $\lambda = 0$, μ is the functional derivative of the free energy $\mathcal{F}[\phi]$, and the dynamics is in detailed balance with respect to the Gibbs-Boltzmann measure, and the station-

ary probability of observing a configuration $\phi(x)$ is given by $P_s[\phi] \propto \exp(-\mathcal{F}[\phi]/\epsilon)$. In this case, the relative stability of the phases ϕ_H and ϕ_I can be inferred from the values of $\mathcal{F}[\phi_H]$ and $\mathcal{F}[\phi_I]$. Transitions between these states involve a reaction path passing through a saddle-point configuration on $\mathcal{F}[\phi]$.

In contrast, when $\lambda \neq 0$, TRS is broken because μ does not satisfy the Schwarz condition on its functional derivative [25, 36, 37]. Consequently, the stationary distribution of the system is no longer available. Therefore, $\mathcal{F}[\phi]$ provides no information on the relative stability of ϕ_H and ϕ_I. Instead, characterizing their relative stability relies on dynamics.

Phase transitions and quasipotential– We use Freidlin-Wentzell large-deviation theory (LDT) to compute transition rates from ϕ_H to ϕ_I and vice versa, along with most likely paths [12], in the limit as $\epsilon \to 0$ (when the system is either in ϕ_H or ϕ_I with probability one, and proper phases can be defined). Denoting $k_{I,H}$ as the rate to transition from ϕ_I to ϕ_H, it is given by $k_{I,H} \asymp \exp\left(-V_{\phi_I}(\phi_H)/\epsilon\right)$, where $V_{\phi_I}(\phi_H)$ is the quasipotential of ϕ_H relative to ϕ_I, akin to a potential barrier in Arrhenius' law. A similar expression holds for $k_{H,I}$, the rate from ϕ_H to ϕ_I. Assessing the relative stability of the phases relies on the difference in the logarithm of the escape rates:

$$\epsilon \log k_{I,H} - \epsilon \log k_{H,I} \asymp -V_{\phi_I}(\phi_H) + V_{\phi_H}(\phi_I), \qquad (3)$$

This expression is positive when ϕ_H is preferred and negative when ϕ_I is. The quasipotential values $V_{\phi_I}(\phi_H)$ and $V_{\phi_H}(\phi_I)$ depend on system control parameters like λ and ϕ_0, thus their difference can switch sign, indicating a first-order phase transition (FOPT). This allows for analyzing these transitions by computing these quasipotentials for various λ and ϕ_0 values, as suggested in [38]. These quasipotentials are obtained as minima of the action functional $S_T[\phi]$, defined as:

$$S_T[\phi] = \int_0^T \int_\Omega |\nabla^{-1}(\partial_t\phi - \nabla^2\mu)|^2 dx dt \qquad (4)$$

where Ω denotes the domain. Minimizing action (4) with respect to both T and ϕ, subject to $\phi(t=0,x) = \phi_H$ and $\phi(t=T,x) = \phi_I$ yields $V_{\phi_H}(\phi_I)$, and subject to $\phi(t=0,x) = \phi_I$ and $\phi(t=T,x) = \phi_H$ yields $V_{\phi_I}(\phi_H)$.

Deep gMAM– The key feature of the method, introduced in [34], is to replace the field $\phi(x,t)$ with an ansatz satisfying the spatio-temporal boundary conditions and involving deep neural networks. The minimization of (4) is achieved by a stochastic gradient descent (SGD) algorithm where space-time collocation points are randomly drawn at each SGD step. Such procedure is very often used in problems involving PINNs. The method is simple to implement, highly flexible, and, importantly, able to tackle problems in higher dimensions not accessible by classical approaches. Furthermore, it provides an analytical parametric approximation of the various fields across the entire spatio-temporal domain.

In this study, results from the deep gMAM algorithm in $d = 1$ were validated against those from classical gMAM implementation, which discretizes the field in space and time and is somewhat more intricate. For further details on both algorithms, especially regarding optimization on T via reparametrization of the solution using arc-length s instead of physical time t, we refer to the Supplemental Material (SM) [39].

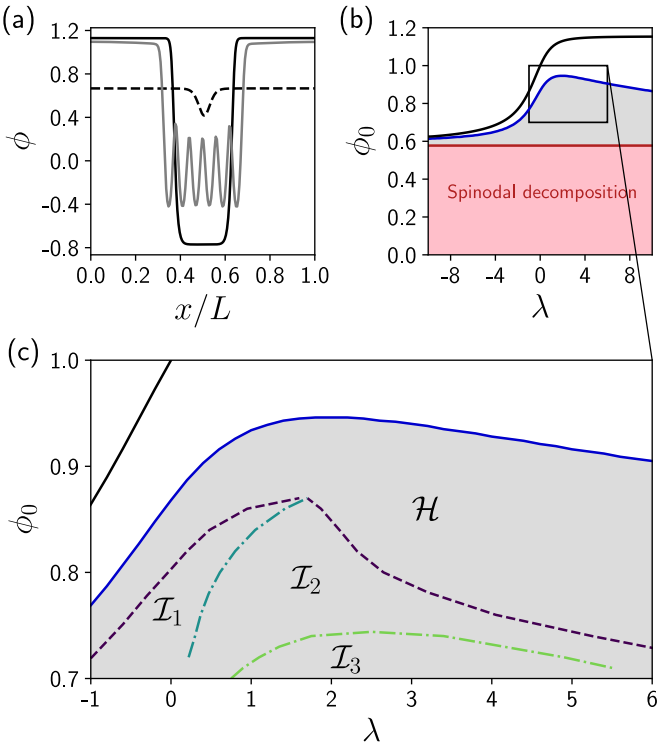

FIG. 1. (a) Three configurations in $d = 1$: The solid line represents the stable inhomogeneous state ϕ_I, the dashed line indicates the unstable critical state $\phi_{c,1}$, and the grey line depicts a field configuration along the nonequilibrium reaction path from ϕ_I to the homogeneous state ϕ_H (not shown). Parameters: $\phi_0 = 0.65$, $\lambda = 2$, and $L = 120$. (b) Phase diagram of active Model B in parameter space (λ, ϕ_0). It shows the binodal (black line) and the spinodal (red line) previously computed in [22]. In finite-size systems, the bistable region does not fully span between the spinodal and the binodal but stops at the blue line (shown here for $L = 60$ and $d = 1$). Both states ϕ_H and ϕ_I are stable in the shaded region. (c) In the bistable region, the purple dashed line marks the FOPT between ϕ_H and ϕ_I. On this line, $V_{\phi_H}(\phi_I) = V_{\phi_I}(\phi_H)$. In region $\mathcal{H}$, ϕ_H is thermodynamically preferred, in regions $\mathcal{I}_1$, $\mathcal{I}_2$, $\mathcal{I}_3$, the inhomogeneous state ϕ_I is preferred. The index q in $\mathcal{I}_q$ indicates the number of bumps along the reaction path from ϕ_I to ϕ_H. Region $\mathcal{I}_3$ may display asymmetric paths with slightly smaller actions than their symmetric counterparts.

Phase diagram in 1d– We focus first on the one-dimensional system, whose dynamics reads

$$\partial_t\phi = -\partial_x^2[\partial_x^2\phi + \phi - \phi^3 - \lambda(\partial_x\phi)^2] + \partial_x\xi, \qquad (5)$$

with $\langle \xi(x,t)\xi(x',t')\rangle = 2\epsilon\delta(t-t')\delta(x-x')$. Space has been rescaled such that all lengths are given in units of $\sqrt{\nu}$. We consider a system of size L and we take periodic boundary conditions. The relevant parameters are thus L, the total mass $\phi_0 \equiv L^{-1}\int_0^L \phi\, dx$, and the activity level λ. The constant

density solution of Eq. (5) is the homogeneous state ϕ_H, and since the mass ϕ_0 is conserved, we have $\phi_H = \phi_0$. We restrain the study to the region $\phi_0 > 0$, since Eq. (5) is invariant under $(\lambda, \phi) \to (-\lambda, -\phi)$. The homogeneous state ϕ_H is always a stable fixed point of the noiseless dynamics for $\phi_0 > \phi^{\lambda}_{\mathrm{sp}^+}$, where $\phi^{\lambda}_{\mathrm{sp}^+} = 1/\sqrt{3}$ is the frontier of the spinodal in the space (λ, ϕ_0) for $\phi_0 > 0$. We are interested in the region where ϕ_H competes with the inhomogeneous state ϕ_I. In the infinite system size limit, this region lies between the spinodal $\phi^{\lambda}_{\mathrm{sp}^+}$ (red line in Fig. 1(b)) and the binodal curve $\phi^{\lambda}_{\mathrm{bi}^+}$ (black line in Fig. 1(b-c)) that yields the bulk densities of each phase when the system undergoes a phase separation [22, 27]. We will denote by $\phi^{\lambda}_{\mathrm{f.o.}}$ the transition density indicating the change of thermodynamic stability of the two competing metastable states, ϕ_I and ϕ_H. Naturally we have $\phi^{\lambda}_{\mathrm{sp}^+} \leq \phi^{\lambda}_{\mathrm{f.o.}} \leq \phi^{\lambda}_{\mathrm{bi}^+}$.

First, let us recall that for large but finite systems, the phase-separated state cannot be the preferred phase if ϕ_0 is taken too close to the binodal density $\phi^{\lambda}_{\mathrm{bi}^+}$. For instance, in equilibrium, (i.e. $\lambda = 0$) the binodal densities are $\phi^{\lambda=0}_{\mathrm{bi}^{\pm}} = \pm 1$ but a free energy argument that compares interfaces and bulk contributions shows that $\phi^{\lambda=0}_{\mathrm{f.o.}}$ converges to 1 as $\phi^{\lambda=0}_{\mathrm{f.o.}} \sim 1 - (1/L)^{1/2}$. More than that, due to finite-size effects, ϕ_I may not exist at all when there is not enough space in the domain to nucleate the phase separation. Hence, one should keep in mind that in a finite system, say of size L, bistability can only be observed below some threshold density $\phi^{\lambda=0}_{\mathrm{m}^+_L} \leq \phi^{\lambda=0}_{\mathrm{bi}^+}$, represented as the blue curve in Fig. 1. Nonetheless, we have $\phi^{\lambda}_{\mathrm{m}^{\pm}_L} \to \phi^{\lambda}_{\mathrm{bi}^{\pm}}$ as $L \to \infty$. To pinpoint the FOPT, we run the gMAM algorithm for $\phi_0 \in [\phi^{\lambda}_{\mathrm{sp}}, \phi^{\lambda}_{\mathrm{m}^+_L}]$ and $\lambda \in [-10, 10]$. Solving $V_{\phi_H}(\phi_I) = V_{\phi_I}(\phi_H)$ identifies the FOPT line $\phi^{\lambda}_{\mathrm{f.o.}}$, the purple dashed line in Fig. 1(c), which splits the diagram into two regions: for $\phi_0 < \phi^{\lambda}_{\mathrm{f.o.}}$ the thermodynamically stable state is the inhomogeneous one, ϕ_I, while for $\phi_0 > \phi^{\lambda}_{\mathrm{f.o.}}$ the homogeneous state $\phi_H = \phi_0$ is preferred. Interestingly, we also find that the binodal and the FOPT have a reentrance direction along λ that does not exist in the system of infinite size (see Fig. 1(c)).

Reaction paths in 1d– We consider first the reaction path starting from the homogeneous state ϕ_H and reaching ϕ_I, and we compute $V_{\phi_H}(\phi_I)$ for different values of λ and system size L. Interestingly this path is very close to the heteroclinic orbit joining ϕ_H to ϕ_I, and going through the critical (saddle) state $\phi_{c,1}(x)$ that displays one density bump (see Fig. 1(a)) and possesses only one unstable direction. This behavior is very similar to the equilibrium nucleation scenario occurring in the Cahn-Hilliard dynamics, as already noted in [1]: to escape ϕ_H, the system only needs to nucleate a finite size droplet of the opposite phase. The cost for the action associated to this event is always finite, and the value of the action does not differ much from the one computed using the time-reversed relaxational path (a few percent difference, not shown).

In contrast, the transition from ϕ_I to ϕ_H is more complex, and its analysis had never been explored so far. For $\phi_0 > 0$, as λ increases, the reaction path no longer follows the time-reverse relaxation path that goes through the saddle $\phi_{c,1}$, but rather passes close to critical points with a large number of unstable directions, see Fig. 2(a) and 2(b), as it may sometimes be observed in nonequilibrium systems [34, 38]. Any critical points ϕ_c can be obtained by solving the noiseless and stationary version of Eq. (5). It solves $\partial_x^2 \phi_c = -\phi_c + \phi_c^3 + \lambda(\partial_x \phi_c)^2 + \mu_0$, with μ_0 a constant, $L^{-1}\int_0^L \phi_c(x)dx = \phi_0$, and ϕ_c subject to the constraints of periodicity. A Newton mapping similar to the one introduced in [22] enables us to compute precisely the critical points using a symplectic scheme (see SM). For given λ and ϕ_0, pairs of critical points with q bumps ($q \in \mathbb{N}^*$) appear at critical values of the system size denoted $L^{\star}_q$, reported in Fig. 2(c). The saddle-node bifurcation at $L^{\star}_q$ occurs when the system size L is large enough to fit an additional bump on the density profile. For $L = L^{\star}_q$, one degenerate critical state $\phi^{\star}_{c,q}$ becomes accessible to the dynamics. As $L > L^{\star}_q$, the degeneracy is lifted and two distinct critical states of q bumps appear. Any of the states $\phi_{c,q}$ can be decomposed into q identical bumps of size L/q. In particular, the state with bumps of largest amplitude strictly lies in the basin of attraction of ϕ_I, while the other state lies on the separatrix between ϕ_I and ϕ_H. We dis-

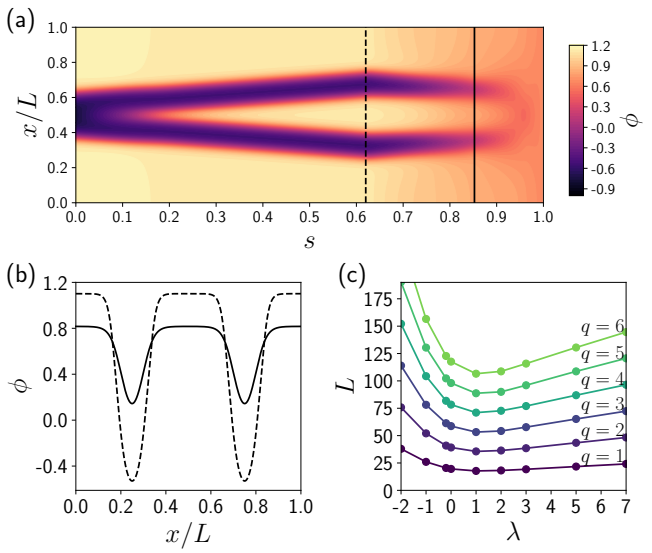

FIG. 2. (a) Minimum action path joining ϕ_I (at $s = 0$) to ϕ_H (at $s = 1$) for $\lambda = 2$, $\phi_0 = 0.65$ and $L = 44.7$ in $d = 1$ dimension. The vertical lines pinpoint the states where the norm of the flow is minimal (and almost zero), corresponding to the states close to the critical points. The corresponding critical points are displayed in panel (b). The state at the dashed line lies in the basin of attraction of the inhomogeneous state, while the state at the solid line lies on the separatrix between the ϕ_I and ϕ_H. The action from the dashed line to the solid line is strictly positive, while the action from the solid line to ϕ_H is zero. (b) Pair of critical states displaying two bumps, for same parameters as panel (a). If $L = L^{\star}_2$, these two states merge in a saddle-node bifurcation. (c) Threshold lengths $L^{\star}_q(\lambda)$ indicating the apparition of critical states with a given number q of bumps as a function of the system activity λ. Above the critical q-line, pairs of critical states with q bumps are dynamically accessible.

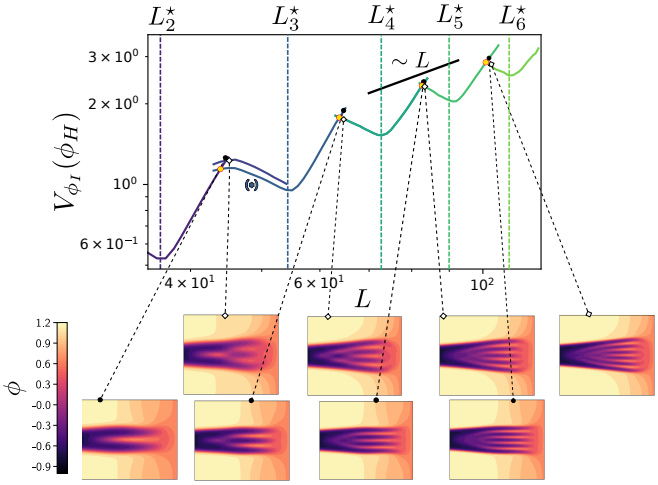

FIG. 3. Minimum action $V_{\phi_I}(\phi_H)$ as a function of the system size L (top panel), for paths starting at ϕ_I and reaching ϕ_H. Here $\lambda = 2$ and $\phi_0 = 0.65$. The action non-monotonically increases because increasing the system size L allows for qualitatively different reaction paths. The successive branches of the curve correspond to different types of paths displaying an increasing number of bumps, see bottom panels. The yellow dots indicate where branches cross each other. The $(*)$ symbol indicates a branch on which the path is no longer axisymmetric (see SM). The vertical dashed lines indicate the critical lengths $L_q^\star$, also given in Fig. 2(c).

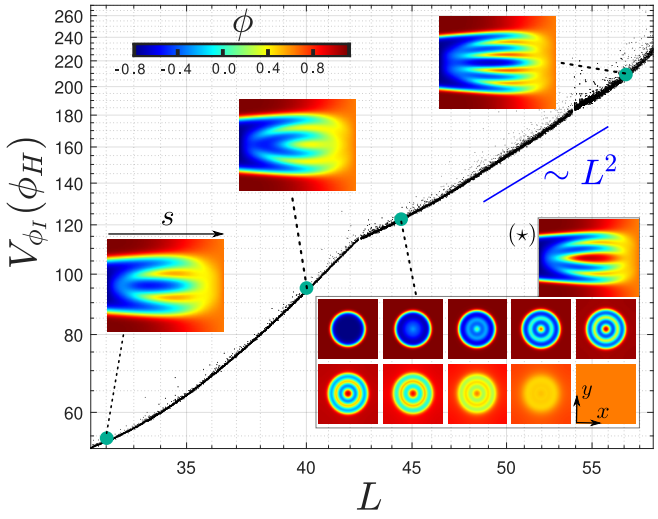

FIG. 4. Minimum action $V_{\phi_I}(\phi_H)$ as a function of L obtained using the deep gMAM method, in $d = 2$ dimensions. The bottom-right panels shows the successive states along the Minimum Action Path joining ϕ_I to ϕ_H for $L = 44.7, \lambda = 2, \phi_0 = 0.65$. The $(\star)$ panel is the same solution in (s, r) coordinates where r is the radial coordinate and s is the arclength coordinate. Other reaction paths in radial coordinates are shown for different values of $L = 32, 40, 57$. They exhibit additional microstructures as L increases.

play an example of such a pair of critical states for $q = 2$ in Fig. 2(b). For all $q \geq 2$, the critical states are of Morse index $q \geq 2$. The case $q = 1$ is special as it corresponds to the apparition of the inhomogeneous metastable state ϕ_I, jointly with the critical state of Morse index 1, $\phi_{c,1}(x)$. A sketch of the structure of the deterministic flow between critical points is given in the SM. In summary, while the path from ϕ_H to ϕ_I indeed resembles the equilibrium one, the path from ϕ_I to ϕ_H displays spatial microstructures which are not present in equilibrium. Notably, the number q of bumps along the instanton changes with L, see Fig. 3, but also depends on ϕ_0 and λ, as indicated by the $\mathcal{I}_q$-labeled regions in Fig. 1. In the SM, we provide a more detailed discussion on the paths selection, and we show that the number of bumps along the path cannot be simply obtained from a spectral analysis.

Phase transitions in 2d and 3d– The reaction paths are also computable in higher dimensions using the deep gMAM algorithm. We specifically examine transitions from ϕ_I to ϕ_H, having also checked that transitions from ϕ_H to ϕ_I are in line with classic nucleation theory [1] (results not shown). In $d = 2$, we investigate the dependence on domain size L, as illustrated in Fig. 4. These transitions display radial symmetry, with microstructures increasing as L grows. The system exhibits extensive action values $V_{\phi_I}(\phi_H)$, scaling as $\sim L^2$. Although the action in Fig. 4 seems monotonic, rescaling it by L^2 reveals a very similar non-monotonic behavior as in one dimension (not shown). Evidence suggests that instantons do not traverse multi-spike profiles, which are numerically identified as critical states of the AMB (see SM and Ref. [40]), as their action values consistently exceed those of the radially symmetric path. Additionally, we compute 3D transitions, with one typical example shown in Fig. 5. These transitions also exhibit radial symmetry. Notably, there is a significant dimensional effect: for same extension L, microstructures have more room to span as dimension increases. This is anticipated due to mass conservation, as the positive mass concentrate towards the domain's corners. It is noteworthy that in dimensions $d \geq 2$, characterizing critical states in Cahn-Hilliard is more challenging [40] than in $d = 1$ [41], and this question remains open for the AMB. Overall, comparing to the Arrhenius law for $\lambda = 0$ reveals that the active term substantially reduces the action required to escape the inhomogeneous state.

Conclusion– We have computed the phase diagram of the AMB in $d = 1$, identified various nucleation scenarios in the binodal, and demonstrated similar instanton phenomenology in $d = 2$ and 3. By computing the reaction paths, we identified regions where the homogeneous state is thermodynamically preferred. The fact that the action $V_{\phi_I}(\phi_H)$ remains extensive in system size, while $V_{\phi_H}(\phi_I)$ remains finite, confirms that eventually, the system should phase-separate as $L \to \infty$ when lying in the binodal region. Our results align with those of Cates and Nardini [1], who showed that nucleation from the homogeneous state in AMB for $d \geq 2$ is qualitatively similar to classical nucleation theory in equilibrium. Moreover, a common feature among all cases is the presence of microstructures with more complex patterns as the dimension d increases. These patterns help decreasing significantly the action required to escape the inhomogeneous state. Our numerical results were obtained using the deep gMAM ap-

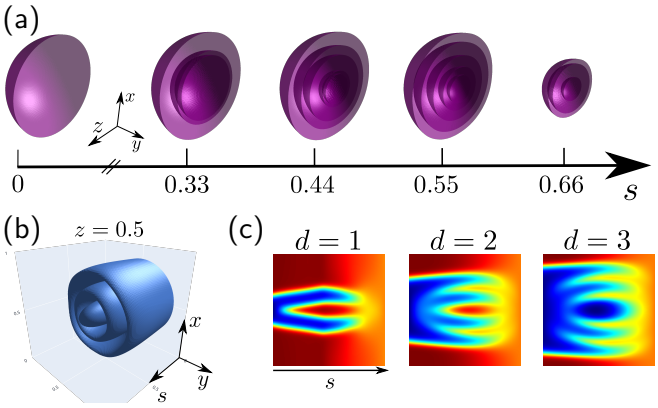

FIG. 5. (a) Isosurfaces $\phi(x, y, z) = 0$ along the reaction path from ϕ_I to ϕ_H, for $d = 3$. A slice is shown at $y = 0.5L$. (b) Isosurface $\phi = 0$ in space (s, x, y) and $z = 0.5L$. (c) Comparison of the reaction paths in space (s, r) for $L = 44.7$ for $d = 1$, 2, and 3. For all panels: $\lambda = 2$, $\phi_0 = 0.65$.

proach [34] and cross-checked in $d = 1$ by running the classical gMAM [30]. While the latter algorithm is more accurate, the discretization scheme adopted for the Cahn-Hilliard equation becomes numerically prohibitive when $d \geq 2$. The deep gMAM approach does not suffer much from an increase in the dimension d. Consequently, we were able to compute transitions for $d = 3$. Overall, these features make the proposed method relevant for numerous active matter systems that may undergo phase separation, and for field theories displaying metastable states in high dimension.

We thank Thibaut Arnoulx de Pirey, Cesare Nardini, Jeremy O'Byrne, and Julien Tailleur for interesting discussions. This work was supported by the Materials Research Science and Engineering Center (MRSEC) program of the National Science Foundation under Grants No. NSF DMR-1420073 and by Grant No. NSF DMR-1710163. R. Z. thanks Laboratoire MSC Paris for hospitality. R. Z. and E. V.-E. would also like to thank the Center for Data Science ENS Paris for hospitality.

[1] M. E. Cates and C. Nardini, Phys. Rev. Lett. **130**, 098203 (2023).
[2] G. M. Torrie and J. P. Valleau, Journal of Computational Physics **23**, 187 (1977).
[3] P. G. Bolhuis, D. Chandler, C. Dellago, and P. L. Geissler, Annual Review of Physical Chemistry **53**, 291 (2002).
[4] T. Grafke and E. Vanden-Eijnden, Chaos: An Interdisciplinary Journal of Nonlinear Science **29**, 063118 (2019).
[5] G. M. Rotskoff, A. R. Mitchell, and E. Vanden-Eijnden, in *Proceedings of the 2nd Mathematical and Scientific Machine Learning Conference* (PMLR, 2022) pp. 757–780.
[6] K. Binder, Reports on Progress in Physics **50**, 783 (1987).
[7] D. Richard, H. Löwen, and T. Speck, Soft Matter **12**, 5257 (2016).
[8] A. K. Omar, K. Klymko, T. GrandPre, and P. L. Geissler, Physical Review Letters **126**, 188002 (2021).
[9] H. A. Kramers, Physica **7**, 284 (1940).
[10] L. Onsager and S. Machlup, Physical Review **91**, 1505 (1953).
[11] W. E, W. Ren, and E. Vanden-Eijnden, The Journal of Chemical Physics **126**, 164103 (2007).
[12] M. I. Freidlin and A. D. Wentzell, *Random Perturbations of Dynamical Systems*, Grundlehren der mathematischen Wissenschaften, Vol. 260 (Springer New York, New York, NY, 1998).
[13] D. Ludwig, SIAM Review **17**, 605 (1975).
[14] R. S. Maier and D. L. Stein, Phys. Rev. Lett. **69**, 3691 (1992).
[15] M. I. Dykman, E. Mori, J. Ross, and P. M. Hunt, The Journal of Chemical Physics **100**, 5735 (1994).
[16] L. Bertini, A. De Sole, D. Gabrielli, G. Jona-Lasinio, and C. Landim, Reviews of Modern Physics **87**, 593 (2015).
[17] F. Bouchet and J. Reygner, Annales Henri Poincaré **17**, 3499 (2016).
[18] T. Grafke, T. Schäfer, and E. Vanden-Eijnden, in *Recent Progress and Modern Challenges in Applied Mathematics, Modeling and Computational Science*, edited by R. Melnik, R. Makarov, and J. Belair (Springer New York, New York, NY, 2017) pp. 17–55.
[19] E. Woillez, Y. Zhao, Y. Kafri, V. Lecomte, and J. Tailleur, Phys. Rev. Lett. **122**, 258001 (2019).
[20] M. Kardar, G. Parisi, and Y.-C. Zhang, Physical Review Letters **56**, 889 (1986).
[21] T. Sun, H. Guo, and M. Grant, Physical Review A **40**, 6763 (1989).
[22] R. Wittkowski, A. Tiribocchi, J. Stenhammar, R. J. Allen, D. Marenduzzo, and M. E. Cates, Nature Communications **5**, 4351 (2014).
[23] C. Nardini, E. Fodor, E. Tjhung, F. van Wijland, J. Tailleur, and M. E. Cates, Phys. Rev. X **7**, 021007 (2017).
[24] M. E. Cates, in *Lecture Notes of the Les Houches Summer School: Volume 112, September 2018*, edited by J. Tailleur, G. Gompper, C. Marchetti, J. M. Yeomans, and C. Salomon (Oxford University Press, 2019).
[25] J. O'Byrne, Phys. Rev. E **107**, 054105 (2023).
[26] M. E. Cates and J. Tailleur, Annual Review of Condensed Matter Physics **6**, 219 (2015).
[27] A. P. Solon, J. Stenhammar, M. E. Cates, Y. Kafri, and J. Tailleur, New Journal of Physics **20**, 075001 (2018).
[28] T. Speck, Physical Review E **105**, 064601 (2022).
[29] W. E, W. Ren, and E. Vanden-Eijnden, Communications on pure and applied mathematics **57**, 637 (2004).
[30] E. Vanden-Eijnden and M. Heymann, The Journal of Chemical Physics **128**, 061103 (2008).
[31] M. Heymann and E. Vanden-Eijnden, Phys. Rev. Lett. **100**, 140601 (2008).
[32] M. Raissi, P. Perdikaris, and G. E. Karniadakis, Journal of Computational Physics **378**, 686 (2019).
[33] G. E. Karniadakis, I. G. Kevrekidis, L. Lu, P. Perdikaris, S. Wang, and L. Yang, Nature Reviews Physics **3**, 422 (2021).
[34] E. Simonnet, Journal of Computational Physics **491**, 112349 (2023).
[35] E. Tjhung, C. Nardini, and M. E. Cates, Physical Review X **8**, 031080 (2018).
[36] T. Grafke, M. E. Cates, and E. Vanden-Eijnden, Physical Review Letters **119**, 188003 (2017).
[37] J. O'Byrne and J. Tailleur, Physical Review Letters **125**, 208003 (2020).
[38] R. Zakine and E. Vanden-Eijnden, Phys. Rev. X **13**, 041044 (2023).
[39] The Supplemental Material can be found at [INSERT LINK]

and includes additional references [42–46]. The codes can be found at https://github.com/rzakine/gMAM_active-Model-B.

[40] P. W. Bates and G. Fusco, Journal of Differential Equations **160**, 283 (2000).

[41] P. W. Bates and P. C. Fife, SIAM Journal on Applied Mathematics **53**, 990 (1993).

[42] D. Donnelly and E. Rogers, American Journal of Physics **73**, 938 (2005).

[43] E. Forest and R. D. Ruth, Physica D: Nonlinear Phenomena **43**, 105 (1990).

[44] W. E, W. Ren, and E. Vanden-Eijnden, Phys. Rev. B **66**, 052301 (2002).

[45] Z. Liu, W. Cai, and J. Z.-Q. Xu, Communications in Computational Physics **28**, 1970 (2020).

[46] D. Kingma and J. Ba, arXiv:1412.6980 (2014).